

Emergence of half-metallic ferromagnetism in transition metal substituted $\text{Na}_{0.5}\text{Bi}_{0.5}\text{TiO}_3$

Chandan Kumar Vishwakarma¹ and B. K. Mani^{1,*}

¹*Department of Physics, Indian Institute of Technology, Hauz Khas, New Delhi 110016, India*

(Dated: July 7, 2023)

The multifunctional materials with prominent properties such as electrical, ferroelectric, magnetic, optical and magneto-optical are of keen interest to several practical implications. In the roadmap of designing such materials, in the present work, using density functional theory based first-principles calculations, we have investigated the functional properties of transition metal substituted-NBT. Our calculations predict the emergence of half-metallic ferromagnetism in the system. A nonzero magnetic moment of $1.49 \mu_{\text{B}}/\text{f.u.}$ is obtained for 25% concentration of Ni. Our data on optical properties for pure NBT is in excellent agreement with available theory and experiments. For Ni-NBT, we observed a diverging nature of static dielectric constant, which could be attributed to the induced metallic character in the material. Our simulations on MOKE predict a significant Kerr signal of 0.7° for 6.25% Ni-concentration.

I. INTRODUCTION

The development of multifunctional materials with two or more properties, such as magnetic, ferroelectric, piezoelectric, and optical, has received a lot of interest in recent years [1–3]. These materials have the potential to revolutionize various industry applications, including healthcare, energy and electronics [4–6]. In the search for such materials, sodium bismuth titanate, $\text{Na}_{0.5}\text{Bi}_{0.5}\text{TiO}_3$ (NBT), has received a remarkable attention than any other lead-free ferroelectrics due to its tendency to show multifunctionality by various mechanisms [7–9]. NBT is a complex perovskite oxide with two cations (Na^+ and Bi^{3+}) on the A-site and one cation (Ti^{2+}) on B-site with a rhombohedral symmetry at room temperature [10]. It exhibits various anomalous properties associated with site-specific substitutions, including improved ferroelectricity and piezoelectricity, magnetism and optoelectronic properties [11, 12].

The presence of Ti at the B site provides a strategy to introduce ferromagnetism by substituting transition-metal (TM) at B-site. In experimental studies, Refs. [13] and [14], ferromagnetism at room temperature was observed for Fe and Co-doped NBT, respectively. In a similar experimental work by Dung *et al.*, a room-temperature ferromagnetism was reported for Ni-doped NBT [15]. The maximum magnetization value reported was around $0.91 \mu_{\text{B}}/\text{Ni}$ for 9% of Ni concentration at 5 K. Moreover, it was also observed in the same study that the optical bandgap decreases with Ni-concentration. However, in a different experimental study, Pradhan *et al.*, the optical band gap was observed to increase with Ni concentrations [16]. The contradictory trend of experimental data suggest the lack of understanding for optical behavior of TM-doped NBT. In addition, to the best of our knowledge, there are no data from theory simulations on probing magnetism in TM-doped NBT. It can thus be

surmised that there is a need for a systematic theoretical study to understand the underlying mechanism behind the multifunctional properties in TM-doped NBT.

The present study aims to probe, with the help of the state-of-the-art of first-principles calculations, the electronic, magnetic, optical and magneto-optical properties of NBT and TM-substituted NBT. More precisely, we aim is to address the following questions: i) What is the impact of Ni substitution on the electrical and optical properties of NBT? ii) Assimilate the mechanism behind the advent of magnetic degrees of freedom in Ni-substituted NBT iii) How this introduced ferromagnetism couples with the dielectric properties of NBT? To assess the coupling between magnetic and optical degrees of freedom, we have examined the linear magneto-optic Kerr effect in the polar geometry, in which the spin and incident photons are perpendicular to the sample surface. This configuration of the Kerr effect is the most favorable way to trace the magneto-optical properties experimentally [17–19].

The texts in the paper are organized in four sections. In Section II, we provide a brief description of the computational methods used in our calculations. In Section III, we present and analyze our results on electronic structure, magnetic, optical, and magneto-optical properties for NBT and Ni-substituted NBT. The summary of our findings is presented in the last Section.

II. COMPUTATIONAL METHODOLOGY

Probing transition metal-substituted NBT structure and emerging properties requires an accurate treatment of interstitial effects in the material at atomic scale. For this, we have performed *ab-initio* spin-polarized calculations using density functional theory (DFT) as implemented in the Vienna *ab-initio* simulation package (VASP)[20, 21]. To account for the exchange correlation among electrons, we used Perdew-Burke-Ernzerhof (PBE) [22] variation of generalized-gradient approxima-

* bkmani@physics.iitd.ac.in

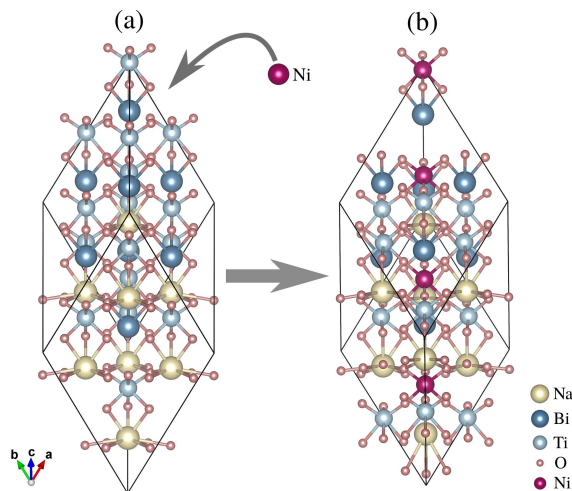


Figure 1. Crystal structures of $\text{Na}_{0.5}\text{Bi}_{0.5}\text{TiO}_3$ (panel (a)) and $\text{Na}_{0.5}\text{Bi}_{0.5}(\text{Ti}_{0.75}\text{Ni}_{0.25})\text{O}_3$ (panel (b)).

tion pseudopotential. And, to account for the strongly correlated $3d$ -electrons of Ni we have incorporated the Hubbard U correction [23] in our calculation. The value, 11.57, of U is computed self-consistently using density functional perturbation theory (DFPT) employing the cococcioni's *et al.* [24] approach. A rhombohedral supercell of size $2 \times 2 \times 2$ with 80-atoms is used to incorporate various concentrations of Ni. All the structures were optimized using full relaxation calculations up to 10^{-4} eV \AA^{-1} force tolerance. For this, we used conjugate gradient algorithm with Monkhorst-Pack [25] k -mesh of $5 \times 5 \times 5$. For the self-consistent-field (SCF) calculations, the Brillouin zone was sampled with $9 \times 9 \times 9$ k -mesh. The energy convergence criterion is maintained at 0.001 meV, whereas the plane wave energy cutoff used was 600 eV. The real and imaginary parts of the dielectric function is calculated using DFPT as implemented in VASP.

III. RESULTS AND DISCUSSIONS

A. Crystal Structure

The structural parameters for pure NBT were taken from the experimental crystal structure (space group $R3c$) data [8] and optimized further through the full relaxation calculations to achieve a minimum energy configuration. Our computed lattice parameters and Wyckoff positions are given in Table I. Computed lattice parameters and Wyckoff positions for NBT are given in Table I. As we observed from the table, our computed lattice parameter 5.65 is in good agreement with the experimental value 5.51 [8]. The reason for slightly larger value could be attributed to the use of GGA functional our calculation [27].

To incorporate various Ni concentrations in

Table I. Computed lattice parameters and Wyckoff positions for NBT. Values given in the parenthesis are the data from the experiment [26].

Lattice Parameters			
$a = b = c = 5.647(5.51)$ (\AA)			
$\alpha = \beta = \gamma = 58.758(59.803)$ ($^\circ$)			
Wyckoff Positions			
Na1 (1a)	0.25644	0.25644	0.25644
Bi1 (1a)	0.77324	0.77324	0.77324
Ti1 (1a)	-0.00056	-0.00056	-0.00056
Ti2 (1a)	0.48900	0.48900	0.48900
O1 (3b)	0.23013	0.72562	-0.76987
O2 (3b)	0.72771	0.21016	-0.27229

$\text{Na}_{0.5}\text{Bi}_{0.5}[\text{Ti}_{1-x}\text{Ni}_x]\text{O}_3$ (Ni-NBT), we used optimized NBT structure and created a $2 \times 2 \times 2$ supercell. And, we investigated the properties for $x = 0.0625, 0.125, 0.1875$, and 0.25 concentrations of Ni. The Ni-NBT structures were fully optimized again using the force tolerance up to the 10^{-5} eV \AA^{-1} . From our simulations we find that all Ni-NBT structures crystallize in rhombohedral ($R3m$) phase. In Fig. 2 Calculated electronic band structure of $\text{Na}_{0.5}\text{Bi}_{0.5}\text{TiO}_3$ (panels (a) and (b)) we have shown the crystal structures for NBT (panel(a)) and 0.25Ni-NBT (panel(b)). The optimized lattice parameters for the chosen concentrations of Ni are given in Table I. Computed lattice parameters and Wyckoff positions for NBT. Values given in the parenthesis are the data from the experiment [26]. To the best of our knowledge, there are no experimental or other theory data for lattice parameters for Ni-NBT available in the literature for comparison.

B. Electronic Structure and Ferroelectric Properties

In Fig. 2 Calculated electronic band structure of $\text{Na}_{0.5}\text{Bi}_{0.5}\text{TiO}_3$ (panels (a) and (b)) we have shown the spin-polarized electronic band structures of NBT (panels (a) and (b)) and 25Ni-NBT crystals (panels (c) and (d)). We chose to report the data for the highest concentration of Ni as it has the largest effect on the computed properties. The corresponding data for other concentrations are, however, provided in the supplementary material. As we observed from the band gap electronic structure at Γ point for both the spin channels. The calculated band gap, 2.57 eV, is in good agreement with the other theoretical value, 2.82, reported in [28]. The observed wide band gaps for both spin channels suggests the semiconducting nature of the NBT crystal, and is consistent with the data reported in the literature [26, 29, 30]. For 25Ni-NBT , however, we

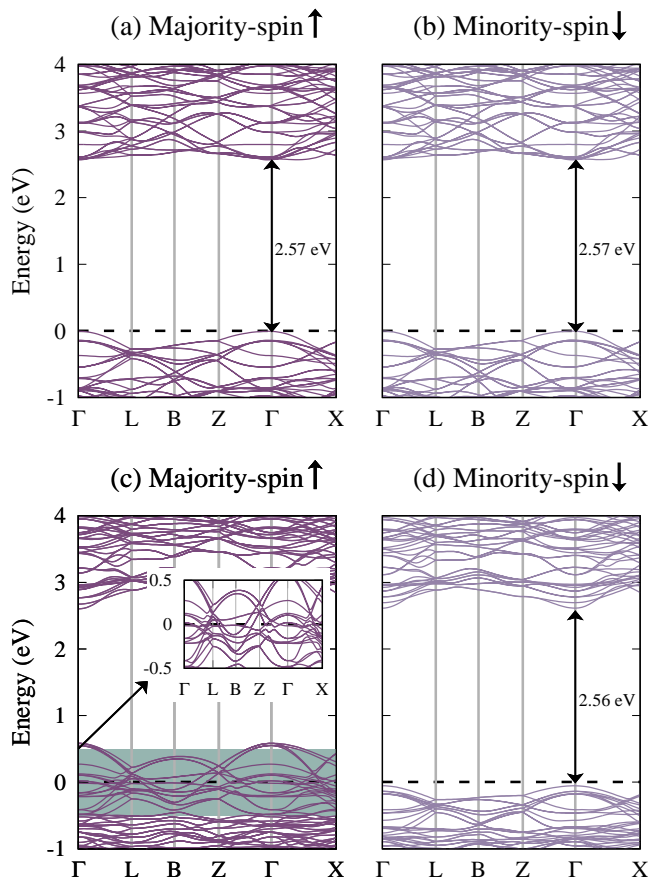


Figure 2. Calculated electronic band structure of $\text{Na}_{0.5}\text{Bi}_{0.5}\text{TiO}_3$ (panels (a), (b)) and $\text{Na}_{0.5}\text{Bi}_{0.5}(\text{Ti}_{0.75}\text{Ni}_{0.25})\text{O}_3$ (panels (c), (d)) for majority and minority spin electrons.

observe an asymmetry in the majority and minority spin channels (panels (c) and (d)). For majority spin, the Fermi level lies in the valence band and shows a metallic nature. Whereas, for minority spin sub band, a large band gap of ~ 2.56 eV is obtained, which resembles the electronic structure of NBT shown in panel (b). This mixed nature of electronic structure indicates a half-metallic character of 25Ni-NBT. A similar electronic structures we also obtain for other concentrations of Ni.

To get further insight into the half-metallicity in Ni-NBT, we examined the atom-projected and orbital-projected electronic structures of NBT and 25Ni-NBT. The data from this for bands and density of states (DoS) are shown in Figs. 3 and 4. The atom-projected band structure of $\text{Na}_{0.5}\text{Bi}_{0.5}(\text{Ti}_{0.75}\text{Ni}_{0.25})\text{O}_3$ for O and Ni atoms for majority (panels (a), (b)) and minority (panels (c), (d)) spin channels are shown in Figs. 3 and 4 respectively. For NBT, as discernible from the panels (a) and (b) of Fig. 3, the valence band for both the spin channels have dominant contributions from O, where $2p$ -electrons contribute the most. For the conduction band, however, the most significant contribution comes from the $3d$ -electrons of

Ti. This observed nature of the electronic structure of NBT is consistent with the reported trend in Refs [29].

For 25Ni-NBT, for majority spin channel, the bands around the Fermi energy are of mixed O and Ni character, with O contribution more prominent than Ni at the Fermi energy (panels (a), (c) in Fig. 3). The atom-projected band structure of $\text{Na}_{0.5}\text{Bi}_{0.5}(\text{Ti}_{0.75}\text{Ni}_{0.25})\text{O}_3$ for O and Ni atoms for majority (panels (a), (b)) and minority (panels (c), (d)) spin channels are shown in Figs. 3 and 4 respectively. This is also consistent with the atom-projected DoS shown in Fig. 4. The density of states and orbital-projected density of states for NBT and 25Ni-NBT are shown in Figs. 5 and 6 respectively. At Fermi energy, O contributes $\approx 70\%$ which mainly comes from $2p$ -electron, whereas the contribution from Ni (mostly from $3d$ -electrons) is about $\approx 20\%$ of the total value. And like NBT, the conduction band is dominated by the $3d$ -electrons of Ti. For minority spin sub band, a significant contribution of O in the valence band below the Fermi level is observed, and comes from the $2p$ -electrons. However, unlike majority spin sub band, there is a negligible contribution from Ni in the bands below the Fermi level. Using the number of electronic states at Fermi level for both spin channels we calculated the spin polarization, which comes out to be 100%. This non-zero electronic states at the Fermi level for majority spin and a wide band gap for minority spin confirms the half-metallicity in Ni-substituted NBT. A similar trend of half-metallicity and spin polarization is also observed for Fe-NBT.

Next, we examine the ferroelectric properties in NBT and Ni-NBT. For this, we calculated the remanent polarization for NBT and Ni-NBT. The electronic contribution to polarization was computed using the Berry phase approach [31, 32]. NBT is a well known lead-free ferroelectric material with experimentally reported remanent polarization as $38 \mu\text{C}/\text{cm}^2$ [10], $32 \mu\text{C}/\text{cm}^2$ [33] and $42.4 \mu\text{C}/\text{cm}^2$ [34] along [001] pseudo-cubic direction. From theory calculations, the reported value of spontaneous polarization, P_S , is $26 \mu\text{C}/\text{cm}^2$ [35]. Our computed value of P_S is $49 \mu\text{C}/\text{cm}^2$. The reason for the difference from experiment could be attributed to the fact that the reported experimental polarizations are at room temperature, whereas the computed values are at 0 K. The spontaneous polarization decreases after the Ni-substitution. We obtained 33.7 and $29.7 \mu\text{C}/\text{cm}^2$ of P_S for 12 and 25% of Ni, respectively. The reason for this decrease could be attributed to the increasing metallic nature due to Ni-substitution.

C. Optical Properties

Next, we examine the optical properties of NBT and Ni-NBT. For this, we calculated the frequency-dependent complex dielectric function using Ehrenreich and Cohen's method [37]. The complex dielectric function is a key parameter and could be useful in probing several fundamental properties of the material. The imaginary part of the dielectric

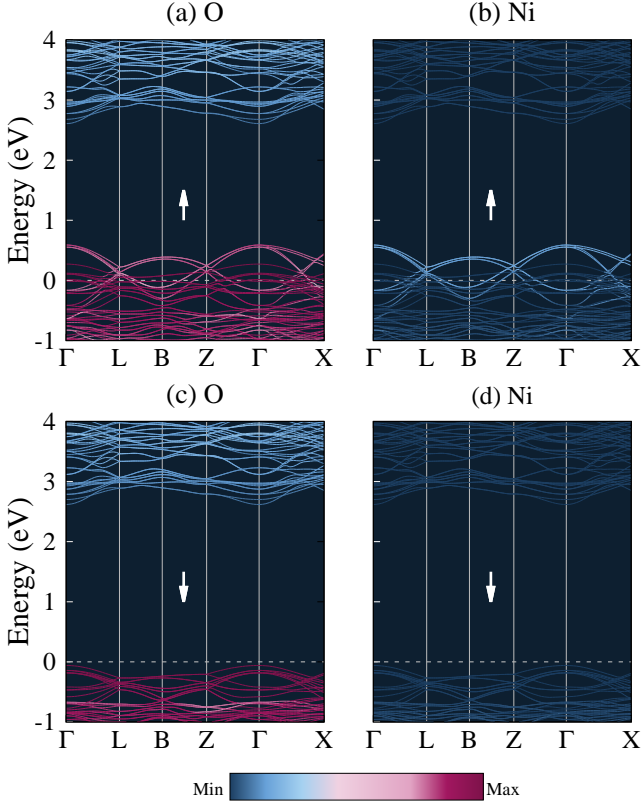


Figure 3. The atom-projected band structure of $\text{Na}_{0.5}\text{Bi}_{0.5}(\text{Ti}_{0.75}\text{Ni}_{0.25})\text{O}_3$ for O and Ni atoms for majority (panels (a), (b)) and minority (panels (c), (d)) spin electrons.

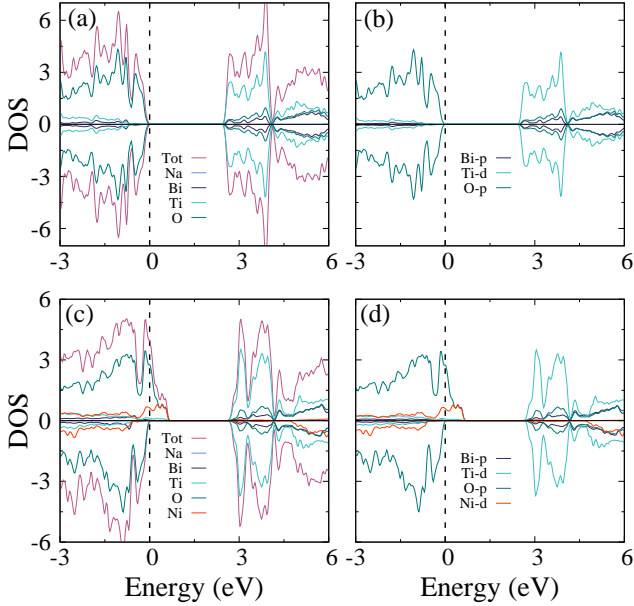


Figure 4. The density of states and orbital-projected density of states for $\text{Na}_{0.5}\text{Bi}_{0.5}\text{TiO}_3$ (panels (a) and (b)) and $\text{Na}_{0.5}\text{Bi}_{0.5}(\text{Ti}_{0.75}\text{Ni}_{0.25})\text{O}_3$ (panels (c) and (d)).

function could be calculated using the linear response theory [38] as

$$\epsilon_2(\omega) = \frac{2\pi e^2}{\epsilon_0 \Omega} \sum_{k,v,c} \delta(E_k^c - E_k^v - \hbar\omega) |\langle \Psi_k^c | \hat{\mathbf{n}} \cdot \mathbf{r} | \Psi_k^v \rangle|^2. \quad (1)$$

Here, the indices k , v and c represent the wave vector, valence and conduction bands, respectively. The states $|\Psi_k^v\rangle$ and $|\Psi_k^c\rangle$ are the wavefunctions associated with valence and conduction bands, respectively, and, E_k^v and E_k^c are the corresponding energies. The constants, e , Ω and ϵ_0 are the charge of the electron, volume of the cell and the permittivity of the free space, respectively. The operator $\hat{\mathbf{n}}$ represents the direction of the applied electric field. The real component of the dielectric constant can be derived from the imaginary component using the Kramers-Kronig relation [38, 39]

$$\epsilon_1(\omega) = 1 + \frac{2}{\pi} P \int_0^\infty \frac{\epsilon_2(\omega') \omega' d\omega'}{\omega'^2 - \omega^2 - i\eta}, \quad (2)$$

where P is the principal value and η is an infinitesimal broadening associated with the adiabatic switching of the dielectric perturbation.

The $\epsilon_1(\omega)$ and $\epsilon_2(\omega)$ for NBT and Ni-NBT from our calculations along with the available experimental data are shown in Fig. 5. The real and imaginary components of the diagonal permittivity of For NBT, as discernible from panels (a) and (b), our calculated real and imaginary components of dielectric function are in good agreement with the experiment [36]. The slight deviation could be attributed to the temperature effects in experiment, as the reported experimental data are at room temperature. Inspecting the real component more closely, the value of static dielectric constant, $\epsilon(0)$, is 6.5. This is consistent with the value reported in previous theory calculation [40] and experiment [36]. This relatively higher value of $\epsilon(0)$ suggests NBT as a potential candidate for light-harvesting applications [41]. The other important characteristic of real spectrum is, negative values at higher energies. This trend is consistent with the previously reported theoretical data [29], and suggests NBT as a potential candidate for plasmonic applications [42].

Examining the imaginary component more closely, we observe one preeminent peak at ~ 4.2 eV and four low-intensity secondary peaks at ~ 5.7 , ~ 6.4 , ~ 7.7 , and ~ 9.0 eV energies. The primary peak originates from the interband transitions from O- $2p$ to Ti- $3d$ and Bi- $6p$ states. The secondary peaks, however, embed major contributions from the O- $2p$ to Na- $2s/2p$ transitions. Our calculated $\epsilon_2(\omega)$ spectrum is in qualitative agreement with the reported theoretical data [29]. The onset of $\epsilon_2(\omega)$ spectrum suggests the optical band gap of NBT as ≈ 2.57 eV, which is consistent with the direct electronic bandgap discussed in previous section.

Considering the case of Ni-NBT, as discernible from the panels (c) and (d), $\epsilon_1(\omega)$ and $\epsilon_2(\omega)$ show a similar trend as NBT at higher energies

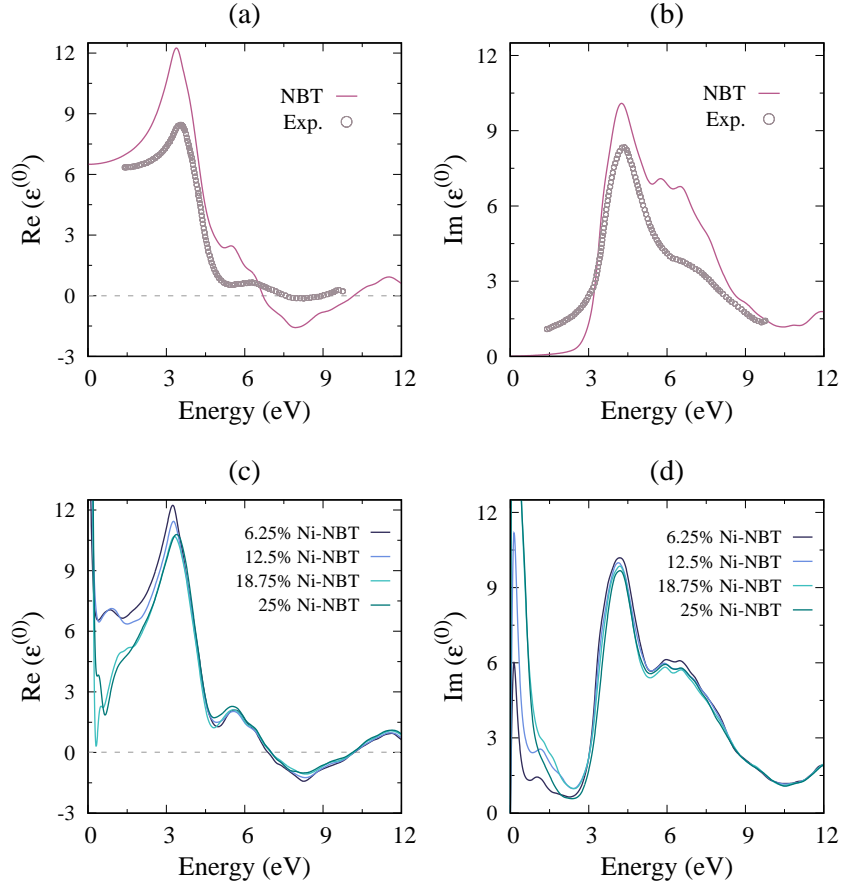


Figure 5. The real and imaginary components of the diagonal permittivity of NBT (panels (a) and (b), respectively) and Ni-substituted NBT (panels (c) and (d), respectively). The experimental data in panels (a) and (b) are from the Ref. [36].

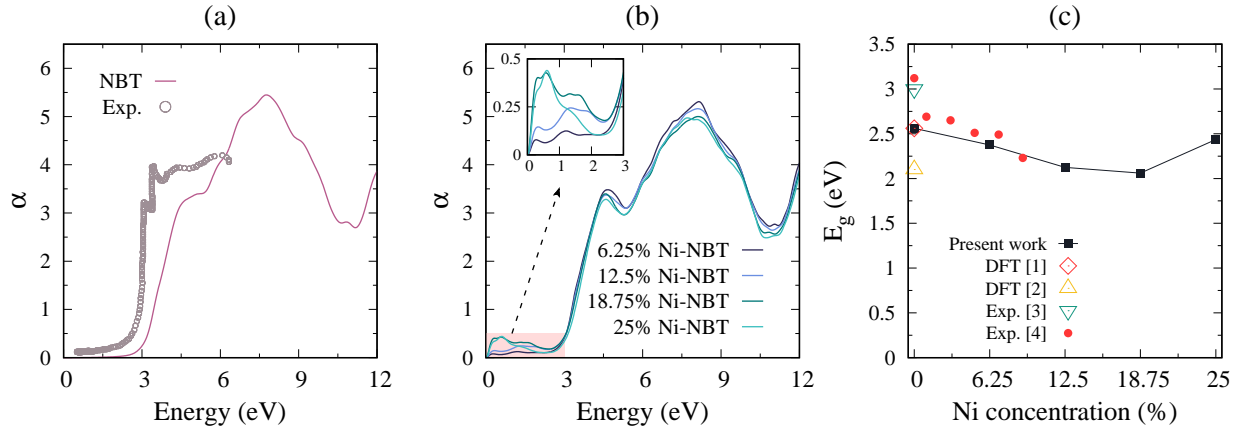


Figure 6. The absorption coefficient of NBT and Ni-substituted NBT (panels (a) and (b), respectively) and optical band gap as function of Ni-concentrations (panel (c)). Refs. [a], [b], [c] and [d] correspond to the works [40], [29], [36] and [15], respectively.

(above 2.5 eV). And, as can be inferred from Fig. 4, the density of states and orbital-projected density of states of $\text{NBT}_{0.95}\text{Bi}_{0.05}\text{TiO}_3$ (panels (a) and (c)) and $\text{NBT}_{0.9}\text{Bi}_{0.1}\text{TiO}_3$ (panels (b) and (d)) are similar. The reason for the observed peaks is attributed to the same interband transitions, O-2p to Ti-3d and Bi-6p. In the low energy regions (below 0.5 eV), however, we observe a diverging nature of $\epsilon_1(\omega)$. The reason for

this could be attributed to the half-metallic nature of $\text{NBT}_{0.95}\text{Bi}_{0.05}\text{TiO}_3$ (panels (a) and (c)) and $\text{NBT}_{0.9}\text{Bi}_{0.1}\text{TiO}_3$ (panels (b) and (d)). It is observed to increase with Ni concentration, and the highest value of ≈ 61 is obtained for 25% concentration. Consistent with the trend of $\epsilon_1(\omega)$, $\epsilon_2(\omega)$ shows sharp peaks below 0.5 eV, with increasing amplitudes with

Ni-concentration.

To get more insight and compare with experimental observations, we have examined the absorption coefficient, α , for NBT and Ni-NBT. In addition, we have extracted the optical bandgap, E_g , for minority spin channel of Ni-NBT at different concentrations using the Tauc's plot [43]. The data from this are shown in Fig. 6. The absorption coefficient of NBT and Ni-substituted NBT (panels (a) and (b), respectively) and optical band gap as function of Ni concentration is shown in Fig. 6. As discernible from the panel (a) of the figure, for NBT, our simulation is in good agreement with the experiment, with a slight shift in the onset of the peak. The reason for this shift could be attributed to the temperature effects in experimental data. For Ni-NBT, on contrary, we observe nonzero peaks in the IR region, which is consistent with the electronic structure data suggesting the half-metallic nature Ni-NBT. Panel (c) shows the optical bandgap for different Ni-concentrations. Consistent with the trend in experiment our computed E_g decreases with Ni concentration. This could be explained in terms of inverse relationship between static dielectric constant and E_g using the Penn model [44]. The increased E_g for 25% concentration could be attributed the decrease in $\epsilon_1(0)$ to 61 from 81 for 18%. Our computed E_g for NBT is close to the previous calculations [40]. The experimental values, Refs. [15, 36], are however on the higher side as they are at finite temperatures.

D. Magnetic Properties

Next, as a probe to magnetic degrees of freedom introduced in the system, we examined the magnetic moments of NBT and Ni-NBT. And, to find the actual ground state magnetic configuration of the system, we probed both ferromagnetic (FM) and antiferromagnetic (AFM) orientations of magnetic moments. From our calculations, we find FM phase as the actual ground state for all concentrations Ni. This is evident from the relative energies of FM and AFM phases given in Table II. Relative energies of FM and AFM configurations, and the atom resolved magnetic moments (in μ_B/atom) for 25% of Ni, where the AFM energy is observed to be larger ≈ 25 meV. In Fig. 7(a) Magnetic moment as function of Ni concentration in Ni-NBT. (b) Octahedral filling of electrons in d -orbitals. The experimental value in panel (a) is from the Ref. [15].

Next, as a probe to magnetic degrees of freedom introduced in the system, we examined the magnetic moments of NBT and Ni-NBT. And, to find the actual ground state magnetic configuration of the system, we probed both ferromagnetic (FM) and antiferromagnetic (AFM) orientations of magnetic moments. From our calculations, we find FM phase as the actual ground state for all concentrations Ni. This is evident from the relative energies of FM and AFM phases given in Table II. Relative energies of FM and AFM configurations, and the atom resolved magnetic moments (in μ_B/atom) for 25% of Ni, where the AFM energy is observed to be larger ≈ 25 meV. In Fig. 7(a) Magnetic moment as function of Ni concentration in Ni-NBT. (b) Octahedral filling of electrons in d -orbitals. The experimental value in panel (a) is from the Ref. [15].

To get more insight into the origin of nonzero magnetic

Table II. Relative energies of FM and AFM configurations, and the atom resolved magnetic moments (in μ_B/atom) for 25Ni-NBT. Contribution from the orbital magnetic moment is given in the parenthesis.

E_{FM} (meV/f.u.)	0
E_{AFM} (meV/f.u.)	24.9
m_{s}^{Ni} (m_{o}^{Ni})	1.539 (0.02)
m_{s}^{O} (m_{o}^{O})	-0.122 (-0.006)
m_{s}^{Ti} (m_{o}^{Ti})	0.036 (0.0)
m_{s}^{Bi} (m_{o}^{Bi})	0.012 (-0.001)
m_{s}^{Na} (m_{o}^{Na})	0.001 (0.0)
m^{Tot} ($\mu_B/\text{f.u.}$)	1.479

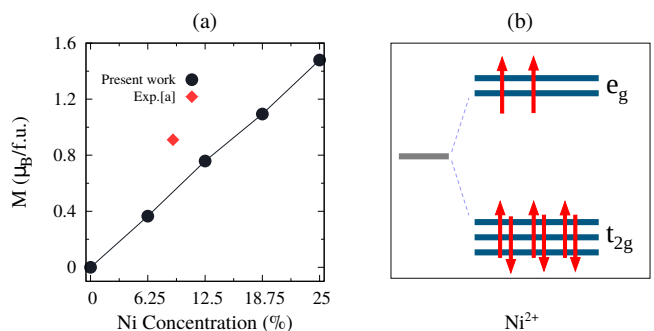


Figure 7. (a) Magnetic moment as function of Ni concentration in Ni-NBT. (b) Octahedral filling of electrons in d -orbitals. The experimental value in panel (a) is from the Ref. [15].

moments in Ni-NBT, we examined separate contributions from each ion. The data from this is tabulated in Table II. Relative energies of FM and AFM configurations, and the atom resolved magnetic moments (in μ_B/atom) for 25% of Ni, where the AFM energy is observed to be larger ≈ 25 meV. In Fig. 7(a) Magnetic moment as function of Ni concentration in Ni-NBT. (b) Octahedral filling of electrons in d -orbitals. The experimental value in panel (a) is from the Ref. [15].

The spin magnetic moment originates from the unpaired $3d$ -electrons in e_g states (panel (b)). The obtained value of spin magnetic moment, $1.54 \mu_B/\text{atom}$, is however smaller than the expected theory value of $2.83 \mu_B/\text{atom}$. The reason for this could be attributed to the strong hybridization between O $2p$ and Ni $3d$ orbitals. Ni is also observed to display a small orbital magnetic moment of $0.02 \mu_B/\text{atom}$ parallel to the spin contribution through SoC. The second dominant contribution is from the O ions. They contribute $\approx -9\%$ of the total value. The opposite contribution from O leads to a decrease in the total magnetic moment. Like Ni, O also has a small parallel contribution from the orbital magnetic moment. Among the other ions, Bi contributes about 2% of total value, whereas Na and Ti has less than 1% contributions.

E. Magneto-optical Properties

The presence of magnetic degrees of freedom in Ni-NBT leads to an anisotropy in the dielectric tensor due to the breaking of time-reversal symmetry. The dielectric tensor for a magnetized material could be written as

$$\epsilon_{ij} = \epsilon_{ij}^{(0)} + \epsilon_{ij}^{(1)}, \quad (3)$$

where $\epsilon_{ij}^{(0)}$ is dielectric tensor in absence of magnetization and $\epsilon_{ij}^{(1)}$ represents the contribution due nonzero magnetization. Within linear in magnetization M , $\epsilon_{ij}^{(1)}$ could be expressed as $\epsilon_{ij}^{(1)} = K_{ijk}M_k$, where K is the magneto-optical coefficient. To examine the magneto-optical properties of Ni-NBT, we computed MOKE spectra in the polar configuration (Fig. 8) Real and imaginary components of magneto-optical permittivity (panels (a) and (b), respectively), Kerr rotation angle (panel

$$\theta_k + i\eta_k = -\frac{K}{\sqrt{\epsilon^{(0)}}(1 - \epsilon^{(0)})}, \quad (4)$$

where $\epsilon^{(0)}$ is the diagonal component of the dielectric tensor in the absence of magnetization. Separating real and imaginary components in Eq. (4equation.3.4), we can derive

$$\theta_k = -\frac{[K_1^2 + K_2^2]^{1/2}}{[\epsilon_1^2 + \epsilon_2^2]^{1/4}[(1 - \epsilon_1)^2 + \epsilon_2^2]^{1/2}} \cos \Theta \quad \text{and} \quad (5)$$

$$\eta_k = -\frac{[K_1^2 + K_2^2]^{1/2}}{[\epsilon_1^2 + \epsilon_2^2]^{1/4}[(1 - \epsilon_1)^2 + \epsilon_2^2]^{1/2}} \sin \Theta, \quad (6)$$

where $\Theta = \tan^{-1}(\frac{K_2}{K_1}) - \frac{1}{2} \tan^{-1}(\frac{\epsilon_2}{\epsilon_1}) - \tan^{-1}(\frac{-\epsilon_2}{1 - \epsilon_1})$. The calculated real and imaginary parts of K and complex Kerr rotation angles for different concentrations of Ni-NBT are shown in Fig 8

Real and imaginary components of magneto-optical permittivity (panels (a) and (b), respectively), Kerr rotation angle (panel (d)), and Kerr ellipticity (panel (c), respectively). Our data on MOKE show significant values of Kerr angles in Ni-NBT, which suggests transition metal substituted-NBT as potential candidates for magneto-optical applications.

As discernible from the panel (d), Kerr rotation shows the same qualitative behavior for all concentrations at higher energies, above ~ 2 eV. There are substantial peaks in both negative and positive y -axes, which are signatures of clockwise and anticlockwise polarizations, respectively, in the material. In the low energy range, below ~ 2 eV, however, we observed a mix trend for θ_k at different concentrations. In the negative y -axis, the most significant peak of amplitude 0.58° is observed at 3.3 eV for 6.5% concentration. The amplitude of the peaks is observed to decrease with Ni-concentration. In the positive y -axis, however, a θ_k reaching up to 0.7° around 10.8 eV is observed for 25% concentration. Unlike the trend for negative θ_k , the peak amplitude for positive θ_k increases with Ni-concentrations.

Fig. 8 Real and imaginary components of magneto-optical permittivity (panels (a) and (b), respectively), Kerr rotation angle (panel (d)), and Kerr ellipticity (panel (c), respectively). Our data on MOKE show significant values of Kerr angles in Ni-NBT, which suggests transition metal substituted-NBT as potential candidates for magneto-optical applications.

IV. CONCLUSIONS

In conclusion, with the help of density functional theory based first-principles calculations, we examined the effect of transition metal substitution on electronic, ferroelectric, magnetic, optical and magneto optical properties of NBT. In agreement with literature, our simulations on electronic properties show NBT as a direct band semiconductor. Our computed bandgap 2.56 eV is within the range of previous theory calculations and experiments. For transition metal substituted-NBT, we observed an emergence of half-metallic ferromagnetism in the system. Our simulation show, while minority spin exhibits a wide bandgap, there are nonzero states at Fermi energy for majority spin. The reason for this could be attributed to the shift in the energy levels of majority spin states due to hybridization between O 2p and Ni 3d states. This asymmetry in the two spin channels lead to an emergence of nonzero permanent magnetic moment in the material. We obtained a magnetic moment of 1.5 μ_B /f.u. for 20% of Ni concentration. For optical properties of NBT, our simulation results are consistent with the available experimental and other theory results. For Ni-NBT, however, we observed a diverging nature of static dielectric constant in the infrared region, which could be attributed to the metallic nature of the material. Our data on MOKE show significant values of Kerr angles in Ni-NBT, which suggests transition metal substituted-NBT as potential candidates for magneto-optical applications.

ACKNOWLEDGMENTS

The authors wish to thank Ravi Kumar, Mohd Zee-shan and Indranil Mal for useful discussions. C. K. V. acknowledges the funding support from Council of Scientific & Industrial Research, India (Grant No. 09/086(1297)/2017-EMR-I). B. K. M. acknowledges the funding support from SERB, DST (CRG/2022/003845). The results presented in the paper are based on the computations using the High Performance Computing clus-

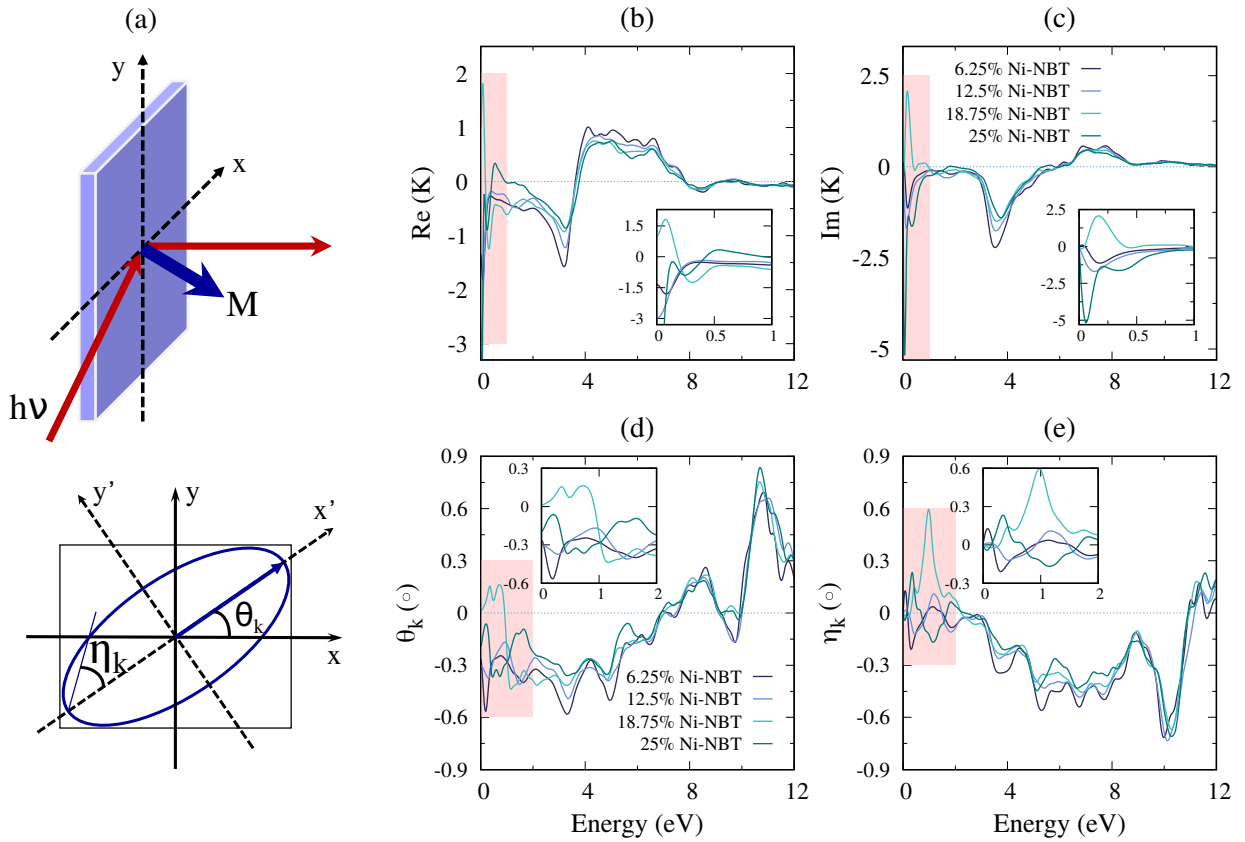


Figure 8. Real and imaginary components of magneto-optical permittivity (panels (a) and (b), respectively), Kerr rotation angle (panel (c)) and Kerr ellipticity (panel (d)) as function of energy.

ter, Padum, at the Indian Institute of Technology Delhi, New Delhi

-
- [1] P. Du, L. Luo, W. Li, Q. Yue, and H. Chen, *Applied Physics Letters* **104**, 152902 (2014).
 - [2] X. Wang, C.-N. Xu, H. Yamada, K. Nishikubo, and X.-G. Zheng, *Advanced Materials* **17**, 1254 (2005).
 - [3] X. Tian, Z. Wu, Y. Jia, J. Chen, R. K. Zheng, Y. Zhang, and H. Luo, *Applied Physics Letters* **102**, 042907 (2013).
 - [4] G.-H. Lee, H. Moon, H. Kim, G. H. Lee, W. Kwon, S. Yoo, D. Myung, S. H. Yun, Z. Bao, and S. K. Hahn, *Nature Reviews Materials* **5**, 149 (2020).
 - [5] Y. Zheng, N. Tang, R. Omar, Z. Hu, T. Duong, J. Wang, W. Wu, and H. Haick, *Advanced Functional Materials* **31**, 2105482 (2021).
 - [6] Y. Huang, C. Zhao, B. Wu, and J. Wu, *ACS Applied Materials & Interfaces* **12**, 23885 (2020).
 - [7] S. B. Vakhrushev, V. A. Isupov, B. E. Kvyatkovsky, N. M. Okuneva, I. P. Pronin, G. A. Smolensky, and P. P. Syrnikov, *Ferroelectrics* **63**, 153 (1985).
 - [8] G. O. Jones and P. A. Thomas, *Acta Crystallographica Section B* **58**, 168 (2002).
 - [9] I. G. Siny, C.-S. Tu, and V. H. Schmidt, *Phys. Rev. B* **51**, 5659 (1995).
 - [10] G. Smolenskii, V. Isupov, A. Agranovskaya, and N. Krainik, *Sov Phys Solid State* **2**, 2982 (1960).
 - [11] A. Mishra, D. K. Khatua, A. De, B. Majumdar, T. Frömling, and R. Ranjan, *Acta Materialia* **164**, 761 (2019).
 - [12] M. Zannen, A. Lahmar, B. Asbani, H. Khemakhem, M. El Marssi, Z. Kutnjak, and M. Es Souni, *Applied Physics Letters* **107**, 032905 (2015).
 - [13] D. Jain Ruth, R. A. U. Rahman, M. Dhamodaran, V. Lakshmanan, S. Balasubramanian, P. Schmid-Beurmann, P. Zhou, G. Srinivasan, and M. Ramaswamy, *Journal of Alloys and Compounds* **830**, 154679 (2020).
 - [14] Y. Wang, G. Xu, X. Ji, Z. Ren, W. Weng, P. Du, G. Shen, and G. Han, *Journal of Alloys and Compounds* **475**, L25 (2009).
 - [15] D. D. Dung, N. Q. Dung, N. B. Doan, N. H. Linh, L. H. Bac, N. N. Trung, N. V. Duc, L. T. H. Thanh, L. V.

- Cuong, D. V. Thiet, and S. Cho, *Journal of Superconductivity and Novel Magnetism* **33**, 911 (2020).
- [16] S. K. Pradhan and S. De, *Ceramics International* **44**, 15181 (2018).
- [17] M. Bastjan, S. G. Singer, G. Neuber, S. Eller, N. Aliouane, D. N. Argyriou, S. L. Cooper, and M. Rübhausen, *Phys. Rev. B* **77**, 193105 (2008).
- [18] X. S. Xu, T. V. Brinzari, S. Lee, Y. H. Chu, L. W. Martin, A. Kumar, S. McGill, R. C. Rai, R. Ramesh, V. Gopalan, S. W. Cheong, and J. L. Musfeldt, *Phys. Rev. B* **79**, 134425 (2009).
- [19] A. Malakhovskii, S. Gnatchenko, I. Kachur, V. Piryatinskaya, A. Sukhachev, and I. Gudim, *Journal of Alloys and Compounds* **542**, 157 – 163 (2012).
- [20] G. Kresse and J. Furthmüller, *Computational Materials Science* **6**, 15 (1996).
- [21] G. Kresse and J. Furthmüller, *Phys. Rev. B* **54**, 11169 (1996).
- [22] J. P. Perdew, K. Burke, and M. Ernzerhof, *Phys. Rev. Lett.* **77**, 3865 (1996).
- [23] V. I. Anisimov, J. Zaanen, and O. K. Andersen, *Phys. Rev. B* **44**, 943 (1991).
- [24] M. Cococcioni and S. de Gironcoli, *Phys. Rev. B* **71**, 035105 (2005).
- [25] H. J. Monkhorst and J. D. Pack, *Phys. Rev. B* **13**, 5188 (1976).
- [26] M. Benyoussef, H. Zaari, J. Belhadi, Y. El Amraoui, H. Ez-Zahraouy, A. Lahmar, and M. El Marssi, *Journal of Rare Earths* **40**, 473 (2022).
- [27] C. Stampfl and C. G. Van de Walle, *Phys. Rev. B* **59**, 5521 (1999).
- [28] H. Lü, S. Wang, and X. Wang, *Journal of Applied Physics* **115**, 124107 (2014).
- [29] M. Zeng, S. W. Or, and H. L. W. Chan, *Journal of Applied Physics* **107**, 043513 (2010).
- [30] S. Behara, G. S. Priyanga, and T. Thomas, *Materials Today Communications* **24**, 101348 (2020).
- [31] R. D. King-Smith and D. Vanderbilt, *Phys. Rev. B* **47**, 1651 (1993).
- [32] R. Resta, *Rev. Mod. Phys.* **66**, 899 (1994).
- [33] H. Yu and Z.-G. Ye, *Applied Physics Letters* **93**, 112902 (2008).
- [34] H. S. Mohanty, T. Dam, H. Borkar, A. Kumar, K. K. Mishra, S. Sen, B. Behara, B. Sahoo, and D. K. Pradhan, *Ferroelectrics* **517**, 25 (2017).
- [35] M. K. Niranjana, T. Karthik, S. Asthana, J. Pan, and U. V. Waghmare, *Journal of Applied Physics* **113**, 194106 (2013).
- [36] B. Andriyevsky, J. Suchanicz, C. Cobet, A. Patryn, N. Esser, and B. Kosturek, *Phase Transitions* **82**, 567 (2009).
- [37] H. Ehrenreich and M. H. Cohen, *Phys. Rev.* **115**, 786 (1959).
- [38] M. Gajdoš, K. Hummer, G. Kresse, J. Furthmüller, and F. Bechstedt, *Phys. Rev. B* **73**, 045112 (2006).
- [39] U. Kreibitz, *Zeitschrift für Physik* **234**, 307 (1970).
- [40] C. K. Vishwakarma and B. K. Mani, *Journal of Applied Physics* **133**, 225703 (2023).
- [41] G. Sudha Priyanga and T. Thomas, *Journal of Alloys and Compounds* **750**, 312 (2018).
- [42] A. Shabani, M. Tsegay Korsa, S. Petersen, M. Khazaei Nezhad, Y. Kumar Mishra, and J. Adam, *Advanced Photonics Research* **2**, 2100178 (2021).
- [43] J. Tauc, R. Grigorovici, and A. Vancu, *physica status solidi (b)* **15**, 627 (1966).
- [44] D. R. Penn, *Physical Review* **128**, 2093 – 2097 (1962).
- [45] S. Picozzi, A. Continenza, M. Kim, and A. J. Freeman, *Phys. Rev. B* **73**, 235207 (2006).
- [46] D. Sangalli, A. Marini, and A. Debernardi, *Phys. Rev. B* **86**, 125139 (2012).